



Ni₃S₂@polypyrrole composite supported on nickel foam with improved rate capability and cycling durability for asymmetric supercapacitor device applications

Lu Long¹, Yadong Yao^{1,*}, Minglei Yan¹, Hongjing Wang^{2,*}, Guanggao Zhang¹, Menglai Kong¹, Lin Yang¹, Xiaoming Liao¹, Guangfu Yin¹, and Zhongbing Huang¹

¹College of Materials Science and Engineering, Sichuan University, Chengdu, Sichuan 610065, China

²West China Second University Hospital, Sichuan University, Chengdu, Sichuan 610065, China

Received: 9 August 2016

Accepted: 21 October 2016

Published online:

28 October 2016

© Springer Science+Business Media New York 2016

ABSTRACT

Ni₃S₂@polypyrrole/nickel foam (Ni₃S₂@PPy/NF) composite was successfully synthesized by combining a facile hydrothermal synthesis and a simple electrochemical-deposited process. For comparative study, the honeycomb-shaped Ni₃S₂ had in situ been grown on NF without the addition of any nickel salt to obtain the Ni₃S₂/NF composite. The electrochemical measurement results show that the area capacitance of the Ni₃S₂@PPy/NF electrode is 1.13 F cm⁻² that is slightly lower than 1.26 F cm⁻² of the Ni₃S₂/NF electrode at a high current density of 30 mA cm⁻², yet its rate capability and cycling stability are far better than those of the Ni₃S₂/NF electrode. Meanwhile, an asymmetric supercapacitor on the basis of the Ni₃S₂@PPy/NF anode and the AC cathode exhibits a high energy density and power density of 17.54 Wh kg⁻¹ and 179.33 W kg⁻¹ at 2.5 mA cm⁻², respectively; besides, the energy density is still 8.67 Wh kg⁻¹ at a power density of 3587.41 W kg⁻¹ even at 50 mA cm⁻². Moreover, the capacitances of the device remain unchanged after 3000 galvanostatic charge/discharge cycles at a high current density of 30 mA cm⁻². Furthermore, two such 1 cm² devices connected in series can light five 40-mW LED indicators or power one of the same-power LED indicator for 20 min after being fully charged. The results demonstrate that our asymmetric supercapacitor has a promising potential in commercial applications.

Address correspondence to E-mail: yaoyd523@163.com; whjscdx@163.com

Introduction

Considering economic and environmental requirements, the search for novel high-performance energy storage devices has become more and more important. Energy storage devices, in particular supercapacitors, a new class of electrochemical energy storage device, have recently received considerable attention because they can store more energy than conventional capacitors and provide higher power than rechargeable battery [1–3]. Besides, supercapacitors have been widely used in numerous areas, including hybrid electric vehicles, mobile electronic devices, military device, and memory backup systems [4, 5].

Unfortunately, lower energy densities of supercapacitors, compared with lithium ion battery, have restricted their practical applications [4]. Hence, improvement of the energy density of supercapacitors is of vital importance to meet the future energy demands. As we all know, specific capacitance and operating voltage of capacitor devices are two key parameters for their energy density, which can be calculated based on the following equation: $E = 1/2 CV^2$, where E , C , V represent energy density, specific capacitance, and operating voltage, respectively [6, 7]. In this case, maximizing specific capacitance and operating voltage of the device can greatly increase the energy density of capacitors. Note that the capacitors with organic electrolytes can provide a wider voltage window than the aqueous electrolyte-based capacitors, but the high cost, high toxicity, and poor ionic conductivity of organic electrolytes limit their applications to some extent [4, 8]. On the other hand, aqueous electrolytes have higher ionic conductivities and are environmentally robust and easy to handle, but they suffer from narrow window of operation voltage of less than 1 V [1, 9]. To solve this problem, a novel device, asymmetric supercapacitor, which can make full use of a battery-type Faradaic electrode (positive electrode) and a capacitor-type electrochemical double-layer electrode (negative electrode), is designed to enlarge the operation voltage by combining two different potential windows in the same aqueous electrolyte [10–13].

In addition, augmentation of the energy density of supercapacitors can also be achieved via improving the specific capacitance of the electrode materials. Till now, numerous efforts have been devoted to studying various electrode materials with high specific

capacitance, good rate capability, and long cycle life. Generally, electrode materials used in capacitors can be classified into three major groups: carbonaceous materials [14–19], conducting polymers [20–24] and transition metal compounds [25–29]. Thereinto, transition metal compounds have been widely investigated because they store energy depending on reversible faradic reactions at the electrode/electrolyte interface. Among the multitudinous pseudocapacitive materials, metal sulfides (e.g., NiS_x , CoS_x , and CuS_x) have been subject to extensive research in recent decades, due to their excellent intrinsic properties and good electrochemical performance [30]. Hereof, nickel sulfides, one of important member of the metal sulfides, have recently aroused increasing attention due to its relatively high theoretical capacity, good electrical conductivity, and cost effectiveness [31–33]. Besides, Ni_3S_2 , one of the most important phases of nickel sulfide, has captured intense attention at present due to their high theoretical capacity, excellent rate performance, and abundant availability of source. For instance, Zhou et al. synthesized the Ni_3S_2 nanorod@ $\text{Ni}(\text{OH})_2$ nanosheet core-shell nanostructures on a three-dimensional graphene network, which showed a large specific capacitance of 1037.5 F g^{-1} at 5.1 A g^{-1} and a good cyclic stability [34]. Moreover, droplet-shaped, hollow Ni_3S_2 nanoparticles with a high capacitance of 1022.8 F g^{-1} at scanning rate of 2 mV s^{-1} were successfully prepared on two-dimensional graphene templates by Ou and his co-workers [35]. Therein, they introduced either graphene or nickel foam (NF) framework to increase the conductivity and the contact area of electrode materials. In the recent years, the study of binder-free electrodes for supercapacitors has become a new research trend. To date, there are so many research groups devoting to making active materials in situ grow on NF to improve the capacitive performances, such as the situ grown NiCo_2S_4 nanotube arrays on NF [36] or the burl-like nickel cobalt sulfide on carbon fibers [37]. Therefore, in this study, binder-free electrodes are designed to avoid the addition of additive which will decrease the electrochemical properties of active materials.

In addition, polypyrrole (PPy) has been widely used in supercapacitors because of its high conductivity, storage ability, and good environmental stability [38]. For instance, Bose group established a unique nanoarchitecture involving PPy and graphene which exhibited excellent electrochemical property

[39]. Li et al. fabricated PPy-multiwalled carbon nanotube composites for electrochemical supercapacitors [40]. Therefore, in this work, we develop a facile hydrothermal method and follow an electrochemical deposition to synthesize the Ni_3S_2 @polypyrrole/nickel foam (Ni_3S_2 @PPy/NF) composite, besides, for comparison, the Ni_3S_2 /nickel foam (Ni_3S_2 /NF) was also prepared in the study. The electrochemical measurement results show that the Ni_3S_2 @PPy/NF electrodes manifest enhanced superior rate capability and longer cycle life compared with the Ni_3S_2 /NF electrode. An asymmetric supercapacitor, assembled using Ni_3S_2 @PPy/NF as the positive electrode and activated carbon (AC) as the negative electrode, exhibits a high energy density and power density as well as a good cycling performance to meet the requirements of modern society for energy-storage devices. Furthermore, two of the devices connected in series can power LED indicators even though the size is very small, demonstrating that our supercapacitor prototype can be a promising supercapacitor for practical applications. These findings also supply a new strategy to enhance the rate capability and cycle life of supercapacitors.

Experimental

Preparation of Ni_3S_2 /NF and Ni_3S_2 @PPy/NF composites

All the reagents were of analytical grade and used as received without further purification. Thiourea, hydrochloric acid, absolute ethanol, and potassium hydroxide were purchased from Kelon Chemical Reagent. The acetone was obtained from Changlian Chemical Reagent Co., Ltd. Pyrrole was purchased from Aladdin Industrial Co., Ltd. And deionized water (DI) was used for the whole experimental process.

The Ni_3S_2 /NF composite was synthesized by a facile hydrothermal process without adding any nickel salt. The detailed procedure can be described as follows. Before the typical hydrothermal reaction, the NF substrate was cleaned successively followed by acetone, 6 M HCl, absolute ethanol, and DI and then dried at 70 °C. After the above pretreatment process, several pieces of clean NF (2 cm × 2 cm) were gained to use in the later steps. Meanwhile, 5 mM thiourea (0.04567 g) was dissolved in 120 mL DI to form a clear solution by magnetic stirring. After the solution was stirred for

30 min, the transparent solution and two pieces of clean NF (2 cm × 2 cm) were transferred to a 200 mL Teflon stainless-steel autoclave, heated in an oven at 160 °C for 12 h, and finally cooled to room temperature naturally. The as-obtained products were rinsed with DI and absolute ethanol several times, and then dried at 70 °C for 5 h in vacuum to obtain the Ni_3S_2 /NF electrode. As is well known, PPy has been widely used in supercapacitors to increase the conductivity of electrode materials to improve the electrochemical properties of the supercapacitor. Therefore, the Ni_3S_2 @PPy/NF composite was synthesized by treating the Ni_3S_2 /NF composite and following a simple electrochemical-deposited procedure. The electrochemical potentiostatic deposition process was performed at room temperature on a conventional three-electrode electrochemical workstation consisting of the as-prepared Ni_3S_2 /NF electrode (1 cm² in area), a platinum plate counter electrode (2.25 cm² in area), and Ag/AgCl as a reference electrode. The deposition potential was controlled at 0.8 V, and the deposited time maintained at 50 s. Furthermore, the deposition solution was prepared based on the method reported in a literature [41]. In brief, the transparent deposition solution for the electrodeposition of PPy was prepared by dissolving 0.3355 g pyrrole monomer, 0.4256 g LiClO_4 , and 1.6298 g sodium dodecyl sulfate into 50 mL DI. After the electrochemical deposition process, black PPy film was observed on the surface of the Ni_3S_2 /NF electrode. The mass of active material (Ni_3S_2) is about 6.5 mg, which is derived from the formula: $m = \Delta m \times (M_{\text{Ni}_3\text{S}_2}/2M_{\text{S}}) = \Delta m \times 240/64$. In this study, a control group, subjected to hydrothermal treatment of two pieces of clean NF (2 cm × 2 cm) without thiourea under the same reaction conditions, was designed to determine the mass reduction of NF at 160 °C. Therefore, in this equation, Δm represents the weight increments of NF after hydrothermal process at 160 °C as well as that resulted after combining with the control group, which can be directly calculated through the weight difference between the control sample and the as-prepared electrodes in this paper, where M is the molecular weight or the atomic weight.

Physicochemical characterizations of the as-synthesized composites

The structural analysis of the as-prepared samples was characterized by powder X-ray diffraction (XRD, DX-1000 diffractometer), using a Cu K α radiation in

the 2θ range of 10° – 80° . The morphology and chemical composition of the as-obtained electrode materials were observed with field-emission scanning electron microscopy (FE-SEM, HITACHI S-4800, Japan) and X-ray energy-dispersive spectrometer (EDX, HITACHI, Japan). The morphology and microstructure of the products were also examined with field-emission transmission electron microscopy (FETEM, Tecnai G2 F20 S-TWIN, USA).

The fabrication and electrochemical measurements of electrodes

All electrochemical properties of the as-synthesized electrode materials were performed using a conventional three-electrode system on an electrochemical workstation (CHI660E, Shanghai, Chenhua Co., Ltd, China). A series of in situ grown $\text{Ni}_3\text{S}_2/\text{NF}$ electrodes ($1\text{ cm} \times 1\text{ cm}$) and $\text{Ni}_3\text{S}_2@\text{PPy}/\text{NF}$ electrode ($1\text{ cm} \times 1\text{ cm}$) were directly used as working electrode. A piece of platinum plate ($1.5\text{ cm} \times 1.5\text{ cm}$) and a Hg/HgO electrode were used as the counter and reference electrodes, respectively. 2 M KOH aqueous solution was used as electrolyte. Thereinto, cyclic voltammetry (CV) measurements were carried out in the potential range of 0–0.55 V (vs Hg/HgO) at different scan rates of 5, 10, 20, 30, 40, 50, 100 mV s^{-1} . The galvanostatic charge/discharge (GCD) experiments at various current densities of 2.5, 5, 10, 20, 30, 40, 50 mA cm^{-2} were operated between 0 and 0.55 V (vs Hg/HgO) at room temperature. Electrochemical impedance spectroscopy (EIS) tests were employed by applying an AC voltage with 5 mV amplitude in the frequencies ranging from 100 kHz to 0.01 Hz at the open-circuit potential. The specific gravimetric capacitance and specific area capacitance of electrode materials can be calculated from GCD curves by virtue of the following equations [42, 43]: $C_g = It/m\Delta V$ and $C_a = It/S\Delta V$, where C_g is the specific gravimetric capacitance (F g^{-1}), C_a is the specific area capacitance (F cm^{-2}), I is the discharge current (A), t is the discharge time (s) in the potential drop (ΔV , V) during discharge passage, m is the mass of active materials (g), and S is the geometrical area of electrode (cm^2).

The assembly and electrochemical measurements of asymmetric supercapacitor

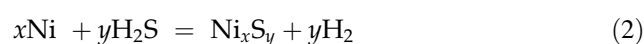
An asymmetric supercapacitor, denoted as the $\text{Ni}_3\text{S}_2@\text{PPy}/\text{NF}$ supercapacitor, was assembled with

the $\text{Ni}_3\text{S}_2@\text{PPy}/\text{NF}$ electrode as the positive electrode and AC as the negative electrode. Moreover, the $\text{Ni}_3\text{S}_2/\text{NF}$ and AC electrodes were also used as the positive electrode and the negative electrode, respectively, to assemble an asymmetric supercapacitor named the $\text{Ni}_3\text{S}_2//\text{AC}$. The electrolyte in the devices is also 2 M KOH aqueous solution, and nonwoven fabrics are used as separator. The assembling processes in detail for the asymmetric supercapacitor are as follows: At first, the as-prepared electrodes were immersed in the 2 M KOH electrode for 12 h to facilitate penetration of the electrolyte. Subsequently, an asymmetric supercapacitor prototype was fabricated relying on the sequence (current collector, anode, separator, cathode, and current collector). Finally, 2 M KOH was dropwise added into the nonwoven until the separator was wetted completely, and then series of electrochemical measurements were conducted in a typical two-electrode system on an electrochemical workstation. Besides, the entire parameter setting and the test methods are similar to that of single electrode, as mentioned above.

Results and discussion

Preparation and physicochemical characterization of the electrode materials

The $\text{Ni}_3\text{S}_2/\text{NF}$ electrode materials were synthesized by a simple and facile in situ growth process which can be briefly expressed as follows [35]:



A photo-macrograph of the pristine NF, $\text{Ni}_3\text{S}_2/\text{NF}$, and $\text{Ni}_3\text{S}_2@\text{PPy}/\text{NF}$ electrode materials were provided in the Supporting Information (Fig. S1a). Obviously, After a typical hydrothermal procedure and a simple electrochemical deposition treatment, a black product, that is, the $\text{Ni}_3\text{S}_2@\text{PPy}/\text{NF}$ electrode material, was obtained. In addition, the silver-colored NF turned gray after hydrothermal reaction being ascribed to the in situ growth of Ni_3S_2 on NF. The $\text{Ni}_3\text{S}_2/\text{NF}$ composite was prepared to explore the influence of the introduction of conducting polymer on the electrochemical properties. Moreover, the scheme for electrode materials preparation had also been provided in the Supporting Information, as

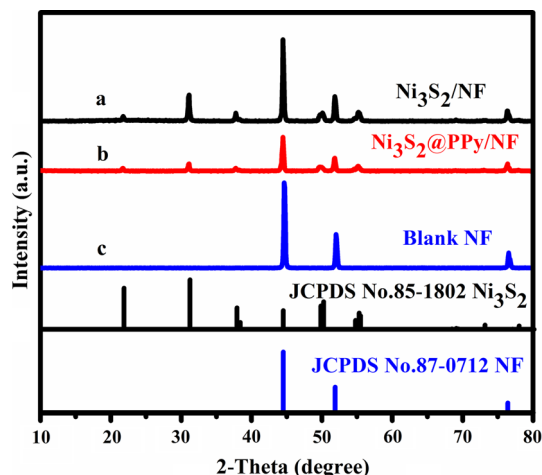


Figure 1 Typical XRD patterns of the $\text{Ni}_3\text{S}_2/\text{NF}$ (a) and $\text{Ni}_3\text{S}_2@\text{PPy}/\text{NF}$ (b) electrode materials as well as the blank nickel foam (c). For comparison, the standard patterns of Ni_3S_2 (JCPDS No. 85-1802) and NF (JCPDS No. 87-0712) are given.

shown in Fig. S1b, which vividly shows the preparation process of the electrode materials in this paper.

Figure 1 depicts a representative XRD pattern of the as-prepared $\text{Ni}_3\text{S}_2/\text{NF}$ and $\text{Ni}_3\text{S}_2@\text{PPy}/\text{NF}$ composites as well as the pristine NF. Distinctly, three characteristic diffraction peaks in Fig. 1c can be attributed to the blank NF (JCPDS 87-0712). The crystalline structure of the $\text{Ni}_3\text{S}_2/\text{NF}$ electrode was analyzed by XRD as shown in Fig. 1a. Apparently, the diffraction peaks in Fig. 1a can be indexed to Ni_3S_2 (JCPDS 85-1802) except three characteristic peaks located at 44.5° , 51.9° , and 76.4° which belong to the pristine NF, confirming that $\text{Ni}_3\text{S}_2/\text{NF}$ has

been successfully synthesized after hydrothermal process. Figure 1b displays the XRD pattern of the $\text{Ni}_3\text{S}_2@\text{PPy}/\text{NF}$ electrode material. Obviously, all of the diffraction peaks in Fig. 1b are the same as that of Fig. 1a, while there are no diffraction peaks for the PPy. Through careful analysis and discussion, it is possible that the content of the PPy is too small to detection. Moreover, no other impure diffraction peaks are detected in Fig. 1a and b, revealing the high purity of samples. What's more, pretty high peak intensity of the diffraction peaks implies that the as-synthesized products have a good crystallinity.

Energy-dispersive X-ray spectrometry mapping analysis was also carried out to further investigating the composition of the $\text{Ni}_3\text{S}_2@\text{PPy}/\text{NF}$ electrode material. Figure 2 shows the EDX elemental mapping images of the $\text{Ni}_3\text{S}_2@\text{PPy}/\text{NF}$ composite. It is quite clear that C, O, N, S, and Ni elements are found in Fig. 2, indicating that Ni_3S_2 has in situ grown on NF, besides, PPy film has also been successfully deposited on the $\text{Ni}_3\text{S}_2/\text{NF}$ composite. That is, the $\text{Ni}_3\text{S}_2@\text{PPy}/\text{NF}$ electrode material has been obtained in this study. Furthermore, EDX spectra of the $\text{Ni}_3\text{S}_2/\text{NF}$ and the $\text{Ni}_3\text{S}_2@\text{PPy}/\text{NF}$ composites are also provided as shown in Fig. S2. Figure S2a depicts the EDX spectrum of $\text{Ni}_3\text{S}_2/\text{NF}$, bringing out the existence of Ni and S elements, namely, Ni_3S_2 has in situ grown on the NF substrate (proved by XRD result). The EDX spectrum of the $\text{Ni}_3\text{S}_2@\text{PPy}/\text{NF}$ composite shown in Fig. S2b contains C, O, N, S, and Ni elements, revealing that the $\text{Ni}_3\text{S}_2@\text{PPy}/\text{NF}$ composite has been successfully synthesized (in agreement with EDX

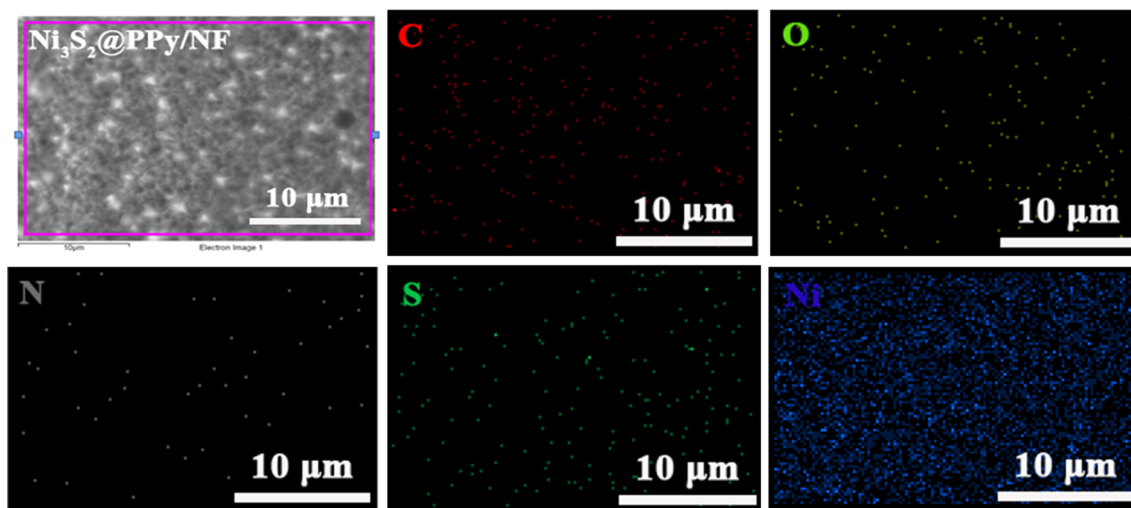


Figure 2 EDX elemental mapping images of the $\text{Ni}_3\text{S}_2@\text{PPy}/\text{NF}$ composite.

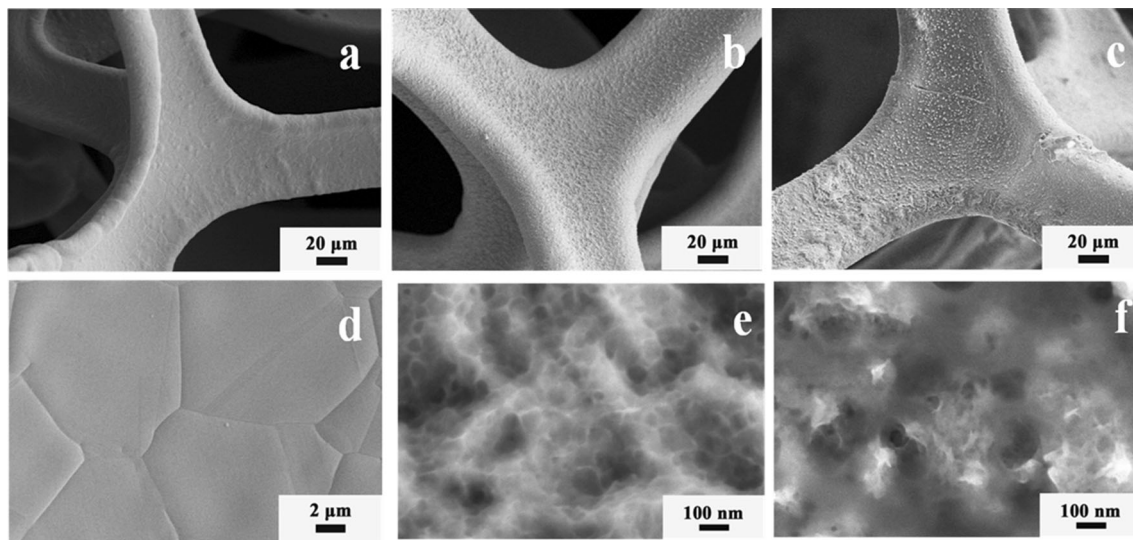


Figure 3 Different magnification FESEM images of the blank nickel foam (a, d), $\text{Ni}_3\text{S}_2/\text{NF}$ (b, e), and $\text{Ni}_3\text{S}_2@\text{PPy}/\text{NF}$ (c, f) electrode materials.

elemental mapping analysis). In a word, the $\text{Ni}_3\text{S}_2/\text{NF}$ and the $\text{Ni}_3\text{S}_2@\text{PPy}/\text{NF}$ composites have been obtained based on the above mentioned results.

FESEM images of the pristine NF and the as-obtained products at different magnifications are shown in Fig. 3. Obviously, a typical three-dimensional (3D) open-pore and crosslinked grid structure of the blank NF can be clearly observed in Fig. 3a, which facilitates easy access of electrolyte ions into the active materials [30]. Moreover, a high-magnification FESEM image of the pristine NF in Fig. 3d exhibits a pretty smooth surface. Figure 3b and e depicts the morphology of the Ni_3S_2 sample supported on NF. A rough surface (Fig. 3b) is detected after the hydrothermal procedure, demonstrating Ni_3S_2 in situ growth on the NF substrate (testified by XRD and EDX results). From the higher magnification FESEM image (Fig. 3e) of the $\text{Ni}_3\text{S}_2/\text{NF}$ electrode, it can be seen that the active material shows honeycomb-shaped that is comprised of crosslinked holes to form a 3D open network-like nanostructure, which is beneficial to the permeation of electrolyte and the transfer of electrons and electrolyte ions. Besides, it can be found that the size of the holes is approximately 50–100 nm. Furthermore, the morphology of the $\text{Ni}_3\text{S}_2@\text{PPy}/\text{NF}$ composite is also observed as shown in Fig. 3c and f. From Fig. 3c, it is evident that the smooth surface of the NF base material roughens after the hydrothermal and the electrodeposited processes. Moreover, it can be noticed that PPy film is found on the surface

of the honeycomb-shaped Ni_3S_2 active material observed from the higher resolution image (Fig. 3f), implying PPy film was successfully electrodeposited on the $\text{Ni}_3\text{S}_2/\text{NF}$ composite. The FESEM results demonstrate that electrode materials with a unique honeycomb-shaped morphology have been acquired after reactions.

FETEM measurement was implemented to further investigate the morphology and structure of the as-prepared products, as shown in Fig. 4. Figure 4a–c depicts the typical FETEM images for the Ni_3S_2 active materials in situ grown on NF which are gained via an ultrasonic treatment. From Fig. 4a–c, it is obvious that a 3D open network-like nanostructure composed of crosslinked holes for the Ni_3S_2 active materials is observed, indicating that the Ni_3S_2 in situ grown on NF has a 3D porous structure which will facilitate the permeation of electrolyte and increase the active sites of electrochemical reactions. From the higher resolution image (Fig. 4c), the size distribution of the Ni_3S_2 electrode material is about 50–100 nm, in agreement with the FESEM result. The $\text{Ni}_3\text{S}_2@\text{PPy}$ electrode material ultrasonically washed from the $\text{Ni}_3\text{S}_2@\text{PPy}/\text{NF}$ composite was also observed shown in Fig. 4d–f. Clearly, it has no significant difference with Ni_3S_2 grown on NF apart from the existence of PPy film. All in all, the FETEM results are in accordance with the above FESEM results, demonstrating a porous structure of the as-synthesized electrode materials, which is beneficial to faradic electrochemical reactions.

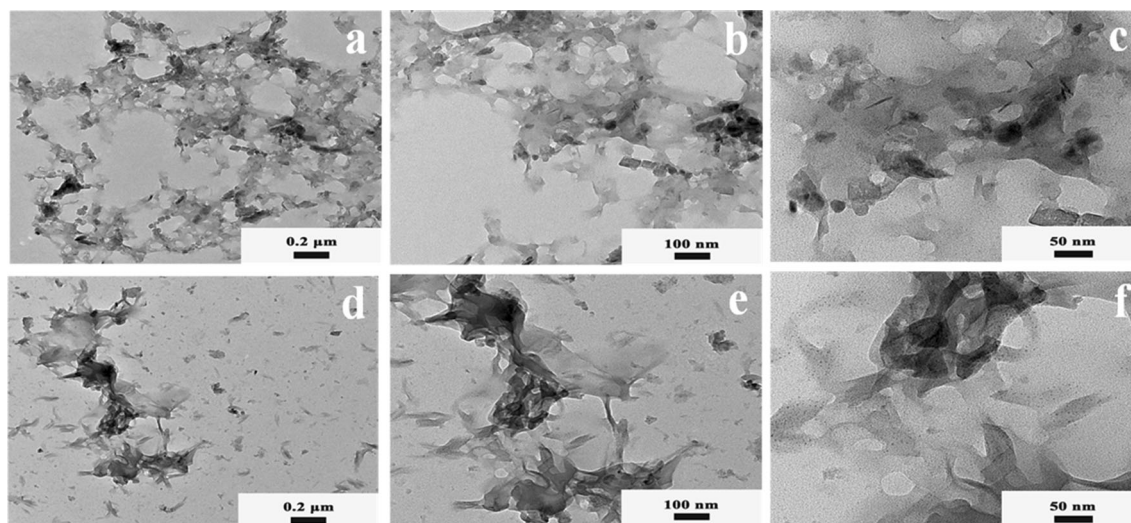
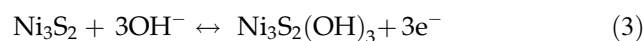


Figure 4 FETEM images of Ni_3S_2 in situ grown on nickel foam (a–c) and the $\text{Ni}_3\text{S}_2@\text{PPy}$ composite deposited on nickel foam (d–f).

Electrochemical properties of the as-prepared working electrodes

Electrochemical performances of the aforementioned electrodes were investigated to determine the charge storage property in a conventional three-electrode system on a CHI 660E electrochemical workstation. Figure 5a exhibits the comparison diagram of CVs of the pristine NF and the as-synthesized electrodes at a scan rate of 10 mV s^{-1} . It can be clearly noticed that the pure NF in the CVs plot is nearly straight line, implying that the contribution of NF to the capacitance of the whole electrode is so small that can be ignored. In addition, the CVs of the $\text{Ni}_3\text{S}_2/\text{NF}$ and the $\text{Ni}_3\text{S}_2@\text{PPy}/\text{NF}$ electrodes at 10 mV s^{-1} can also be found in Fig. 5a. Apparently, a pair of well-defined redox peaks exists in each of the CVs of the as-prepared electrodes, which is because of reversible redox reactions occurred in the electrode surface during the electrochemical process. It is well known that PPy is a typical conducting polymers, which stores energy through the faradaic redox reaction between PPy and electrolyte, indicating its representative pseudocapacitive behavior. The above result reveals that the as-obtained electrodes are of pseudocapacitive type, which are different from normal electric double-layer capacitance, for which the CVs show a rectangular shape. Furthermore, the area of the $\text{Ni}_3\text{S}_2/\text{NF}$ electrode in the CVs is slightly bigger than that of the $\text{Ni}_3\text{S}_2@\text{PPy}/\text{NF}$ electrode at the same scan rate, suggesting that the specific capacitance of the $\text{Ni}_3\text{S}_2/\text{NF}$ electrode is a bit higher than that of the $\text{Ni}_3\text{S}_2@\text{PPy}/\text{NF}$ electrode.

Figure 5b and Fig. S3a show the CVs of the $\text{Ni}_3\text{S}_2@\text{PPy}/\text{NF}$ and the $\text{Ni}_3\text{S}_2/\text{NF}$ electrodes at different scan rates ($5\text{--}100 \text{ mV s}^{-1}$) within a voltage range of $0\text{--}0.55 \text{ V}$ (vs Hg/HgO), respectively. From the CVs, it is obvious that a couple of redox peaks is visible in all CV curves, suggesting reversible redox reactions occurred in the interface between active materials and electrolyte [44]. Moreover, the CVs are almost symmetric, revealing the excellent electrochemical reversibility of the as-synthesized electrode materials. In addition, the current response increases with the increasing scanning rates, and the shapes of CV curves are well retained even at a high scan rate of 100 mV s^{-1} , indicating a good rate capability [34]. Nevertheless, the anodic peaks become more positive, and the cathodic peaks become more negative with the increased scan rate attributing to an increasing polarization at a higher scan rate [45]. The anodic peak in the potential range of $0.45\text{--}0.55 \text{ V}$ (vs Hg/HgO) is because of the conversion of Ni(II) to Ni(III) , while the cathodic peak in the range of $0.25\text{--}0.40 \text{ V}$ (vs Hg/HgO) can be attributed to the reverse process. The reversible redox reactions of $\text{Ni(II)} \leftrightarrow \text{Ni(III)}$ can be described as below [30, 46]:



The GCD measurements were carried out to further explore the electrochemical performances of the electrode materials. Figure 5c shows the galvanostatic charge/discharge curves of the $\text{Ni}_3\text{S}_2@\text{PPy}/\text{NF}$ electrode at a series of current densities ($2.5\text{--}50 \text{ mA cm}^{-2}$) in the potential window of $0\text{--}0.55 \text{ V}$ (vs Hg/HgO). The

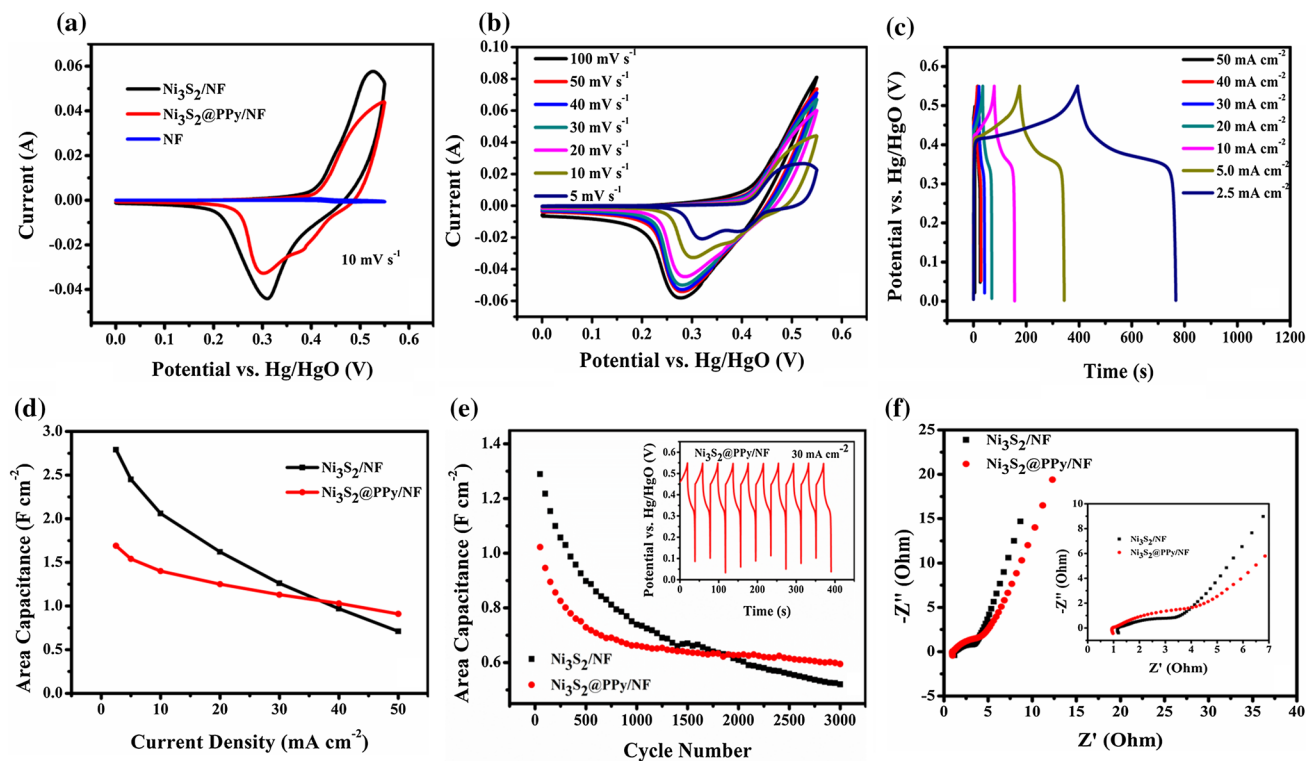


Figure 5 CV curves for the pristine NF, $\text{Ni}_3\text{S}_2/\text{NF}$, and $\text{Ni}_3\text{S}_2@\text{PPy}/\text{NF}$ electrodes under the same scanning rate of 10 mV s^{-1} in 2 M KOH (a). CV curves (b) and charge–discharge curves (c) for the $\text{Ni}_3\text{S}_2@\text{PPy}/\text{NF}$ electrode. The area capacitances of the $\text{Ni}_3\text{S}_2/\text{NF}$ and the $\text{Ni}_3\text{S}_2@\text{PPy}/\text{NF}$ electrodes at different current densities

charge/discharge curves of the $\text{Ni}_3\text{S}_2/\text{NF}$ electrode are also provided in the Supporting Information (Fig. S3b). A plateau region can be distinctly observed during the discharge process as shown in Fig. 5c and Fig. S3b, exhibiting typically pseudocapacitive behaviors of the $\text{Ni}_3\text{S}_2@\text{PPy}/\text{NF}$ and the $\text{Ni}_3\text{S}_2/\text{NF}$ electrodes which is consistent with their CV results [42, 47].

Considering the importance of area capacitance for supercapacitors at practical level, the corresponding area capacitances of electrode materials are provided, which can be calculated relying on the formula mentioned in “Experimental” section. Figure 5d is the comparison diagram of specific area capacitances of the $\text{Ni}_3\text{S}_2@\text{PPy}/\text{NF}$ and the $\text{Ni}_3\text{S}_2/\text{NF}$ electrodes at different current densities. The area capacitances of the $\text{Ni}_3\text{S}_2@\text{PPy}/\text{NF}$ electrode are 1.69, 1.54, 1.40, 1.25, 1.13, 1.03, 0.91 F cm^{-2} at current densities of 2.5, 5, 10, 20, 30, 40 and 50 mA cm^{-2} , respectively. However, the area capacitances of the $\text{Ni}_3\text{S}_2/\text{NF}$ electrode are 2.79, 2.45, 2.06, 1.62, 1.26, 0.97, 0.71 F cm^{-2} at the same current densities. Evidently, the area

(d). Capacitance retention of the as-synthesized samples at a current density of 30 mA cm^{-2} for 3000 charge/discharge cycles (e). Nyquist impedance plots of the $\text{Ni}_3\text{S}_2/\text{NF}$ and the $\text{Ni}_3\text{S}_2@\text{PPy}/\text{NF}$ electrodes (f).

capacitances of the $\text{Ni}_3\text{S}_2@\text{PPy}/\text{NF}$ electrode are a bit lower than that of the $\text{Ni}_3\text{S}_2/\text{NF}$ electrode (in accord with the above CV results) at some current densities, which is attributing to many small bubbles adhered on the surface of the $\text{Ni}_3\text{S}_2@\text{PPy}/\text{NF}$ electrode to hinder the contact between electrolyte and active materials during the electrochemical measurements, leading to the decrease of the area capacitances of the $\text{Ni}_3\text{S}_2@\text{PPy}/\text{NF}$ electrode. Furthermore, the area capacitances of the as-prepared electrodes gradually decrease with the increasing current densities, because OH^- ions in electrolyte diffuse too slowly to meet the demand of mass that OH^- ions required to intercalate swiftly at the interface of electrode/electrolyte at the high current density [48, 49]. It is worth noting that the capacitance of the $\text{Ni}_3\text{S}_2@\text{PPy}/\text{NF}$ electrode still retains 54% of the initial capacitance (1.69 F cm^{-2}) while retaining 25% for the $\text{Ni}_3\text{S}_2/\text{NF}$ electrode when the discharge rate is increased twenty times from 2.5 to 50 mA cm^{-2} , indicating that the rate capability of the $\text{Ni}_3\text{S}_2@\text{PPy}/\text{NF}$ electrode is better than that of the $\text{Ni}_3\text{S}_2/\text{NF}$ electrode (in agreement

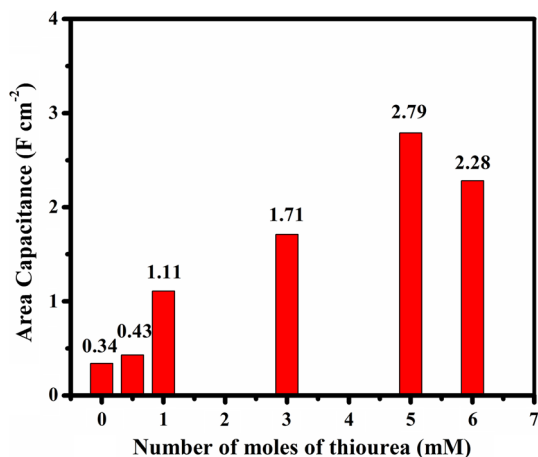


Figure 6 Area capacitances as a function of the number of moles of thiourea for the as-prepared electrodes.

with the variation tendency in Fig. 5d). The results suggest that the introduction of PPy can increase the electrical conductivity of electrode materials and facilitate charge transport between PPy, Ni₃S₂, and NF resulting in the improvement of the rate capability of the Ni₃S₂@PPy/NF electrode [50].

As cycling performance is another crucial factor to evaluate the electrochemical performances of electrodes, the long-term cycle life of the as-prepared

electrodes was also assessed by means of consecutive GCD test carried out at a current density of 30 mA cm⁻² for 3000 cycles. Note that the area capacitances of the Ni₃S₂/NF electrode are reduced continuously during the cycling process, while the area capacitances of the Ni₃S₂@PPy/NF electrode are reduced primarily and remain stable after 1000 cycles. The decrease of the area capacitances during the electrochemical process is ascribed to the peeling off and microstructure variation of the active materials during the fast faradic redox reaction at a high charge/discharge rate [47, 51]. Ultimately, the Ni₃S₂@PPy/NF electrode retains 58.16% of the initial capacitance after 3000 times of cycling as shown in Fig. 5e, which is higher than the value of 40.35% shown for the Ni₃S₂/NF electrode, indicating that the electrochemical stability of the Ni₃S₂@PPy/NF electrode is better than that of the Ni₃S₂/NF electrode. The inset in Fig. 5e depicts GCD curves for the first ten times for the Ni₃S₂@PPy/NF electrode during cycles at 30 mA cm⁻². From the inset, it is known that the GCD curves of the Ni₃S₂@PPy/NF electrode have a good repeatability, indicating that the electrochemical reactions that occurred on the surface of electrode material are highly reversible, resulting in a good cycle life. The above results imply that the

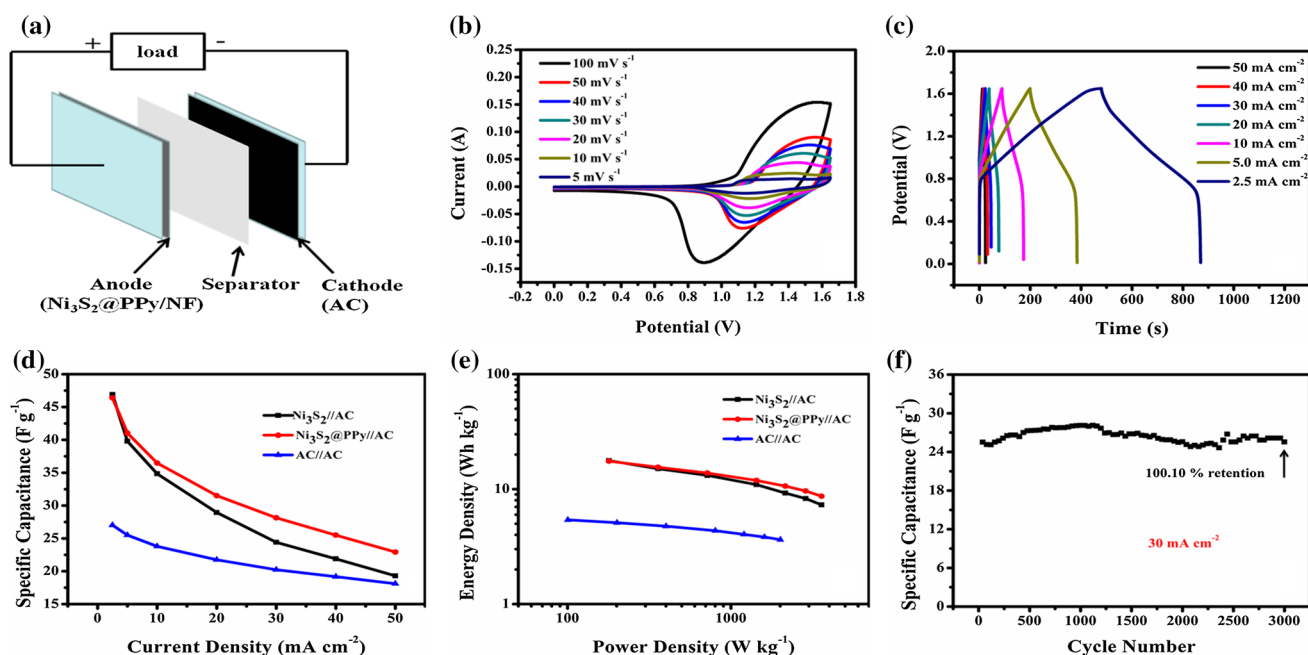


Figure 7 Schematic illustration of the assembled Ni₃S₂@PPy//AC asymmetric supercapacitor device in 2 M KOH electrolyte (a). CV curves (b) and Charge–discharge curves (c) of the Ni₃S₂@PPy//AC asymmetric supercapacitor. Current densities dependence

(d) and Ragone plot (e) of the Ni₃S₂//AC and the Ni₃S₂@PPy//AC asymmetric and AC//AC symmetric supercapacitors. Cycle life of the Ni₃S₂@PPy//AC asymmetric supercapacitor after 3000 cycles at a high current density of 30 mA cm⁻² (f).

introduction of PPy will improve the conductivity of active materials and be beneficial to the transfer of electrons and electrolyte ions, giving rise to the enhancement of cycling stability of electrode materials [52].

EIS technique was also employed at the open-circuit potential in the frequencies ranging from 100 kHz to 0.01 Hz to further characterize the electrochemical properties of the as-prepared electrodes. Figure 5f shows the Nyquist plots of the $\text{Ni}_3\text{S}_2/\text{NF}$ and the $\text{Ni}_3\text{S}_2@\text{PPy}/\text{NF}$ electrodes. Apparently, the impedance spectra exhibit approximately a semicircular shape at the high-frequency region and a slash-like shape at the low-frequency region, which is commonly attributed to the interfacial charge transfer resistance (R_{ct}) between the electrode and the electrolyte as well as Warburg resistance, respectively [53]. It should be noticed that the diameter of the semicircle of the $\text{Ni}_3\text{S}_2/\text{NF}$ electrode at high frequency is slightly smaller than that of the $\text{Ni}_3\text{S}_2@\text{PPy}/\text{NF}$ electrode; besides, the slope of the slash-like shape of the $\text{Ni}_3\text{S}_2/\text{NF}$ electrode at low frequency is slightly steeper than that of the $\text{Ni}_3\text{S}_2@\text{PPy}/\text{NF}$ electrode, indicating that the $\text{Ni}_3\text{S}_2/\text{NF}$ electrode has a larger electroactive surface area, which results in a higher specific capacitance than that of the $\text{Ni}_3\text{S}_2@\text{PPy}/\text{NF}$ electrode (in accordance with CV and GCD results) [54]. In addition, the X-intercept of the Nyquist plots represents the internal resistance (R_e), and the $\text{Ni}_3\text{S}_2@\text{PPy}/\text{NF}$ electrode reflects a R_e value of 0.98 Ω , whereas that of the $\text{Ni}_3\text{S}_2/\text{NF}$ electrode is 1.19 Ω , revealing that the $\text{Ni}_3\text{S}_2@\text{PPy}/\text{NF}$ electrode has a smaller internal resistance, resulting in a higher rate capability and cycling stability [55, 56].

The effect of different active materials on the electrochemical performances

As we all know, active materials are the deciding factor to the electrochemical properties of electrode materials. For this reason, different number of moles of thiourea was investigated in this work to determine the effects of active materials on the electrochemical performances of electrodes. Hereof, number of moles of thiourea with 0, 0.5, 1, 3, and 5 mM was added during the hydrothermal process, respectively, and the as-obtained products were denoted as NS-0, NS-0.5, NS-1, NS-3 and NS-5. Note that NS-5 is the $\text{Ni}_3\text{S}_2/\text{NF}$ electrode researched above. The phases and compositions of the samples were estimated by

XRD as shown in Fig. S4. In the figure, it can be noticed that NS-0 (Fig. S4a) without adding thiourea can be indexed to $\text{Ni}(\text{OH})_2$ (JCPDS 14-0117) and NF (JCPDS 87-0712), yet the content of $\text{Ni}(\text{OH})_2$ is so small that the intensity of diffraction peaks for $\text{Ni}(\text{OH})_2$ is quite low even invisibility. Figure S5 shows the energy-dispersive X-ray spectrum of the NS-0. Clearly, only Ni and O elements can be found in the spectrum, suggesting the existence of $\text{Ni}(\text{OH})_2$. The XRD patterns of NS-0.5, NS-1 and NS-3 can be seen in Fig. S4b, c and d, respectively. Clearly, except the peaks of $\text{Ni}(\text{OH})_2$ and NF, Ni_3S_2 (JCPDS 85-1802) can be found in Fig. S4b. Besides, the intensity of diffraction peaks of Ni_3S_2 increases gradually, while the peaks for $\text{Ni}(\text{OH})_2$ disappear with the increasing amounts of thiourea as shown in Fig. S4c and d. Moreover, the XRD pattern of NS-5 can be observed in Fig. 1a, which is attributed to Ni_3S_2 (JCPDS 85-1802) and NF (JCPDS 87-0712).

FESEM measurements were carried out to further characterize the morphology of the aforementioned as-prepared products. Figure S6 depicts different magnification FESEM images of the as-synthesized samples with different thiourea amounts. Obviously, all of the active materials evenly grow on the NF substrate as shown in Fig. S6a, c, e, and g. A typical sheet shape of NS-0 can be observed in Fig. S6b, while the sheet is a bit thick approximating to 100 nm. Figure S6d exhibits the morphology of NS-0.5, and a flake with the thickness of about several nanometers and some bulks can be found in the picture. The EDX elemental mapping testing finds that the flakes and bulks are attributed to $\text{Ni}(\text{OH})_2$ and Ni_3S_2 , respectively, as shown in Fig. S7, in keeping with the above XRD result. Figure S6f and h show the microtopographic images of NS-1 and NS-3, respectively. It is quite obvious that the morphology of active material transforms to porous structure contributing to the formation of Ni_3S_2 , which is beneficial to the immersion of electrolyte. The FESEM image of NS-5 shown in Fig. 3e displays a more loose porous structure resulting in superior electrochemical properties.

The electrochemical performances of the as-obtained samples prepared by adding different amounts of thiourea were tested via a GCD technique in a three-electrode system at a current density of 2.5 mA cm^{-2} . Figure 6 gives the area capacitances of the as-prepared electrodes obtained by adding different thiourea. The area capacitances of NS-0, NS-

0.5, NS-1, NS-3, NS-5 and NS-6 electrodes calculated by corresponding formulation are 0.34, 0.43, 1.11, 1.71, 2.79 and 2.28 F cm⁻², respectively. Actually, higher number of moles of thiourea added during the hydrothermal process was also prepared in this study, such as 8, 10, 12 mM, and so on. Unfortunately, the as-obtained composites are brittle and given to easy cracking with the increasing amounts of thiourea, which are not suitable as electrode materials. Note that the area capacitance of NS-5 electrode is the biggest, suggesting that the optimal number of moles of thiourea is 5 mM. Taking into account all the above results, it can be noticed that NS-5 electrode, the aforementioned Ni₃S₂/NF electrode, has the optimal electrochemical performance creating the extensive research in this work.

An asymmetric supercapacitor with Ni₃S₂@PPy/NF anode and AC cathode

While the area capacitance of Ni₃S₂@PPy/NF is slightly lower than that of the Ni₃S₂/NF electrode, the rate capability and cycling durability of Ni₃S₂@PPy/NF are superior to those of the Ni₃S₂/NF electrode. Therefore, an asymmetric supercapacitor prototype, Ni₃S₂@PPy//AC, for the sake of convenience, based on Ni₃S₂@PPy/NF as the positive electrode, AC as the negative electrode, and nonwoven fabrics as the separator, was assembled with 2 M KOH aqueous solution as electrolyte. Figure 7a depicts the visual schematic illustration of the Ni₃S₂@PPy//AC asymmetric supercapacitor device. The electrochemical properties of AC single electrode can be seen in the Supporting Information as shown in Fig. S8. The specific capacitance calculated from AC electrode is 188.71 F g⁻¹ at a current density of 2.5 mA cm⁻². Note that the charge balance between the anode and the cathode of the asymmetric supercapacitor is fairly important which is on the basis of the relationship: $q^+ = q^-$. In addition, the stored charges (q) of the electrode can be calculated depending on the equation [12, 31]: $q = C\Delta Vm$, where C is the specific capacitance of electrode, ΔV is the potential window of electrode, and m is the mass of the electrode materials. Consequently, the mass loading of AC in the Ni₃S₂@PPy//AC device is about 5 mg. That is, the total mass of active materials in the two electrodes is 11.5 mg.

The capacitive performances of the as-assembled Ni₃S₂@PPy//AC asymmetric supercapacitor were investigated by CV and GCD measurements in a two-

electrode system on an electrochemical workstation as shown in Fig. 7b and c, respectively. Figure 7b shows the CVs of Ni₃S₂@PPy//AC prototype with a potential window of 0–1.65 V at various scan rates of 5, 10, 20, 30, 40, 50, and 100 mV s⁻¹. As expected, typical redox peaks exist in all the CV curves implying the pseudocapacitive behavior of the as-assembled device. Meanwhile, with the increase of scan rate from 5 to 100 mV s⁻¹, the shapes of CV curves of the capacitor do not change, indicating its good electrochemical performance [31]. Typical galvanostatic charge/discharge curves of the Ni₃S₂@PPy//AC device at different current densities (2.5–50 mA cm⁻²) are provided in Fig. 7c. It can be seen that the voltage of the cell is as high as 1.65 V. Besides, the charge/discharge curves of the capacitor are different from the linear potential response of double electric layer capacitor demonstrating the pseudocapacitive characteristics arising out from the redox reaction within this voltage range of the Ni₃S₂@PPy//AC asymmetric supercapacitor cell (confirmed by CV tests). The corresponding specific capacitance values calculated for the Ni₃S₂@PPy//AC capacitor shown in Fig. 7d are 46.39, 41.04, 36.48, 31.51, 28.14, 25.5 and 22.92 F g⁻¹ at current densities of 2.5, 5, 10, 20, 30, 40, 50 mA cm⁻², respectively. For comparison, the corresponding capacitances of the Ni₃S₂//AC asymmetric and AC//AC symmetric supercapacitors are also provided in Fig. 7d. Apparently, the capacitance value of the Ni₃S₂//AC cell at 2.5 mA cm⁻² is slightly higher than that of Ni₃S₂@PPy//AC; however, the capacitance values of the Ni₃S₂//AC device are smaller than those of Ni₃S₂@PPy//AC when current densities increase to 5.0 mA cm⁻², indicating that our assembled Ni₃S₂@PPy//AC asymmetric cell has a greater rate capability, which is consistent with the single electrode test results. Moreover, capacitances of our prepared asymmetric devices are much bigger than that of AC//AC symmetric supercapacitor. The CV and GCD curves of AC//AC symmetric capacitor are also provided in Fig. S9.

Ragone plots relating the energy density to the power density are an efficient way to evaluate the capacitive performance of the as-assembled capacitors. The formula for energy density has been given above (shown in introduction), and the power density (P) can be calculated by the equation [9, 43]: $P = E/\Delta t$, where E is the energy density, and Δt is the discharge time. Figure 7e illustrates Ragone plots relative to the

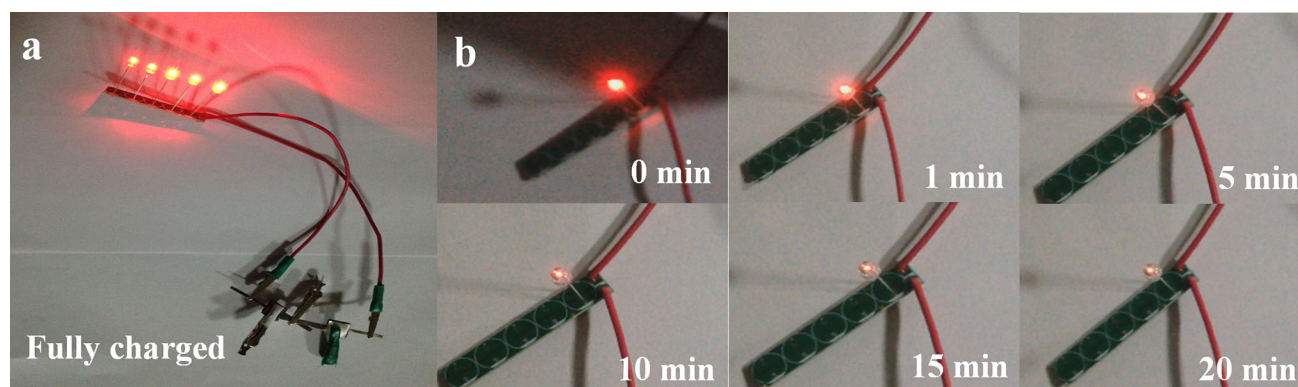


Figure 8 A picture showing that two asymmetric supercapacitors in series can light up five LED indicators (40 mW) after fully charged (a). Pictures of a same power LED indicator at different stages after two asymmetric supercapacitors in series charging to 3.3 V (b).

corresponding energy and power densities with current densities in the range of 2.5–50 mA cm⁻² of the Ni₃S₂//AC and the Ni₃S₂@PPy//AC asymmetric supercapacitors as well as AC//AC symmetric supercapacitor. It is worth noting that the energy density and power density of the Ni₃S₂@PPy//AC asymmetric supercapacitor at 2.5 mA cm⁻² are 17.54 Wh kg⁻¹ and 179.33 W kg⁻¹, respectively, which are little lower than those of the Ni₃S₂//AC asymmetric supercapacitor (17.73 Wh kg⁻¹ and 179.32 W kg⁻¹, correspondingly), but the energy densities of the Ni₃S₂@PPy//AC cell are higher than those of the Ni₃S₂//AC with the increase of current densities, keeping pace with the specific capacitances result. Evidently, energy and power densities of asymmetric devices are much higher than those of AC//AC symmetric supercapacitor (5.4 Wh kg⁻¹ and 100.29 W kg⁻¹, correspondingly). The corresponding energy densities and power densities of the AC//AC symmetric supercapacitor at different current densities are provided in Table S1 seen in Supporting Information. Furthermore, at a higher charge/discharge current density of 50 mA cm⁻², the energy density of the Ni₃S₂@PPy//AC device reaches 8.67 Wh kg⁻¹ at a power density of 3587.41 W kg⁻¹. Obviously, 49.43% of the energy density of the asymmetric supercapacitor is retained when the discharge rate is increased twenty times from 2.5 to 50 mA cm⁻², implying that the energy density of the as-fabricated asymmetric supercapacitor is relatively stable.

The cycle life is another essential factor to weigh the electrochemical property of an energy storage system. Figure 7f shows the specific capacitance of the Ni₃S₂@PPy//AC asymmetric supercapacitor as a function of cycle number at a high current density of

30 mA cm⁻² between 0 and 1.65 V for 3000 cycles. It is easy to notable that the specific capacitance gradually increases until reaching the maximum value during the initial 1250 cycles attributing to the full activation of electrode materials [42, 57]. Then the specific capacitance reduces slightly and basically keeps steady at subsequently repeated GCD cycles. At last, the capacitance retention of the device is 100.10% after 3000 repeated GCD tests at a high current density of 30 mA cm⁻², revealing that our Ni₃S₂@PPy//AC asymmetric supercapacitor has a good cycle life which is highly desired in practical applications.

To further evaluate the practical stored charge ability of our Ni₃S₂@PPy//AC asymmetric supercapacitor, two asymmetric supercapacitors in series were assembled, and the devices could easily light five red LED indicators (40 mW) after charging to 3.3 V at a charge/discharge current density of 2.5 mA cm⁻² even though the dimension of each supercapacitor is only 1 cm² (Fig. 8a). In addition, photographs of a red LED indicator (40 mW) at different lighting time as shown in Fig. 8b. It can be clearly observed that the light of the red LED indicator gradually darkens as time goes by, nevertheless the light of the LED is effective enough for indicator after lighting 20 min. The above results indicate the potential applications of our Ni₃S₂@PPy//AC asymmetric supercapacitor prototype in supercapacitor devices.

Conclusions

We have successfully in situ grown honeycomb-shaped Ni₃S₂ on the NF substrate through a facile one-pot hydrothermal method and synthesized the

Ni₃S₂@PPy/NF composite combining a simple electrodeposited process. The area capacitance of the Ni₃S₂@PPy/NF composite can maintain 54% of the initial capacitance (1.69 F cm⁻²) while 25% for the Ni₃S₂/NF electrode when the discharge rate is increased twenty times from 2.5 to 50 mA cm⁻², indicating that the introduction of PPy conducting film can improve the rate capability of electrode materials. Besides, the cycling durability of the Ni₃S₂@PPy/NF electrode is better than that of the Ni₃S₂/NF electrode. These results imply that combining the electrode materials with PPy is one way to enhance the rate capability and cycling stability of electrodes. Considering the more excellent capacitance performances of the Ni₃S₂@PPy/NF electrode, an asymmetric supercapacitor cell based on Ni₃S₂@PPy/NF and AC was assembled, which exhibits a high energy density and power density. What's more, the capacitance of the as-fabricated prototype cycled repeatedly in the voltage range of 0–1.65 V retains 100.10% of the initial capacitance after 3000 charge/discharge cycles at a high current density of 30 mA cm⁻². Two such devices connected in series can light LED indicators after charging to 3.3 V. These results suggest that our Ni₃S₂@PPy//AC asymmetric supercapacitor cell is a promising candidate for future energy storage applied in hybrid electric vehicles and electric vehicles.

Acknowledgements

The support of the Sichuan Province through a Key Technologies Research and Development Program of Sichuan Province (2011 gz0110) is gratefully acknowledged.

Electronic supplementary material: The online version of this article (doi:10.1007/s10853-016-0529-9) contains supplementary material, which is available to authorized users.

References

- [1] Lu XH, Yu MH, Wang GM, Zhai T, Xie SL, Ling YC, Tong YX, Li Y (2013) H-TiO₂@MnO₂/H-TiO₂@C core-shell nanowires for high performance and flexible asymmetric supercapacitors. *Adv Mater* 25:267–272
- [2] Yuan LY, Xiao X, Ding TP, Zhong JW, Zhang XH, Shen Y, Hu B, Huang YH, Zhou J, Wang ZL (2012) Paper-based supercapacitors for self-powered nanosystems. *Angew Chem Int Ed* 51:4934–4938
- [3] Liu JP, Jiang J, Cheng CW, Li HX, Zhang JX, Gong H, Fan HJ (2011) Co₃O₄ Nanowire@MnO₂ ultrathin nanosheet core/shell arrays. *Adv Mater* 23:2076–2081
- [4] Chang J, Jin MH, Yao F, Kim TH, Le VT, Yue HY, Gunes F, Li B, Ghosh A, Xie SH, Lee YH (2013) Asymmetric supercapacitors based on graphene/MnO₂ nanospheres and graphene/MoO₃ nanosheets with high energy density. *Adv Funct Mater* 23:5074–5083
- [5] Jeong HK, Jin MH, Ra EJ, Sheem KY, Han GH, Arepalli S, Lee YH (2010) Enhanced electric double layer capacitance of graphite oxide intercalated by poly(sodium 4-styrenesulfonate) with high cycle stability. *ACS NANO* 4:1162–1166
- [6] Gao S, Sun YF, Lei FC, Liang L, Liu JW, Bi WT, Pan BC, Xie Y (2014) Ultrahigh energy density realized by a single-layer β-Co(OH)₂ all-solid-state asymmetric supercapacitor. *Angew Chem Int Ed* 53:12789–12793
- [7] Bai MH, Bian LJ, Song Y, Liu XX (2014) Electrochemical codeposition of vanadium oxide and polypyrrole for high-performance supercapacitor with high working voltage. *ACS Appl Mater Interfaces* 6:12656–12664
- [8] Hall PJ, Mirzaeian M, Fletcher SI, Sillars FB, Rennie AJR, Shitta-Bey GO, Wilson G, Cruden A, Carter R (2010) Energy storage in electrochemical capacitors: designing functional materials to improve performance. *Energy Environ Sci* 3:1238–1251
- [9] Wang JG, Yang Y, Huang ZH, Kang FY (2013) A high-performance asymmetric supercapacitor based on carbon and carbon-MnO₂ nanofiber electrodes. *Carbon* 61:190–199
- [10] Sun GZ, Zhang X, Lin RZ, Yang J, Zhang H, Chen P (2015) Hybrid fibers made of molybdenum disulfide, reduced graphene oxide, and multi-walled carbon nanotubes for solid-state, flexible, asymmetric supercapacitors. *Angew Chem Int Ed* 54:4651–4656
- [11] Lu XH, Zeng YX, Yu MH, Zhai T, Liang CL, Xie SL, Balogun MS, Tong YX (2014) Oxygen-deficient hematite nanorods as high-performance and novel negative electrodes for flexible asymmetric supercapacitors. *Adv Mater* 26:3148–3155
- [12] Yan J, Fan ZJ, Sun W, Ning GQ, Wei T, Zhang Q, Zhang RF, Zhi LJ, Wei F (2012) Advanced asymmetric supercapacitors based on Ni(OH)₂/graphene and porous graphene electrodes with high energy density. *Adv Funct Mater* 22:2632–2641
- [13] Lin HL, Liu F, Wang XJ, Ai YN, Yao ZQ, Chu L, Han S, Zhuang XD (2016) Graphene-coupled flower-like Ni₃S₂ for a free-standing 3D aerogel with an ultra-high electrochemical capacity. *Electrochim Acta* 191:705–715

- [14] Xie K, Qin XT, Wang XZ, Wang YN, Tao HS, Wu Q, Yang LJ, Hu Z (2012) Carbon nanocages as supercapacitor electrode materials. *Adv Mater* 24:347–352
- [15] Zhuang XD, Zhang F, Wu DQ, Forler N, Liang HW, Manfred Wagner, Gehrig D, Hansen MR, Laquai F, Feng XL (2013) Two-dimensional sandwich-type, graphene-based conjugated microporous polymers. *Angew Chem Int Ed* 52:9668–9672
- [16] Zhuang XD, Zhang F, Wu DQ, Feng XL (2014) Graphene coupled schiff-base porous polymers: towards nitrogen-enriched porous carbon nanosheets with ultrahigh electrochemical capacity. *Adv Mater* 26:3081–3086
- [17] Zhuang XD, Feng XL (2016) Silicon-compatible carbon-based micro-supercapacitors. *Angew Chem Int Ed* 55:6136–6138
- [18] Qiu YF, Cheng ZY, Guo B, Fan HB, Sun SF, Wu T (2014) Preparation of activated carbon paper through a simple method and application as a supercapacitor. *J Mater Sci* 50:1586–1593. doi:10.1007/s10853-014-8719-9
- [19] Chen AB, Yu YF, Xing TT, Wang RJ, Zhang Y, Li Q (2015) Synthesis of graphitic carbon spheres for enhanced supercapacitor performance. *J Mater Sci* 50:5578–5582. doi:10.1007/s10853-015-9106-x
- [20] Huang KJ, Wang L, Liu YJ, Wang HB, Liu YM, Wang LL (2013) Synthesis of polyaniline/2-dimensional graphene analog MoS₂ composites for high-performance supercapacitor. *Electrochim Acta* 109:587–594
- [21] Zhao WX, Hou ZS, Yao ZQ, Zhuang XD, Zhang F, Feng XL (2015) Hypercrosslinked porous polymer nanosheets: 2D RAFT agent directed emulsion polymerization for multi-functional applications. *Polym Chem* 6:7171–7178
- [22] Zhuang XD, Zhao WX, Zhang F, Cao Y, Liu F, Bi S, Feng XL (2016) A two-dimensional conjugated polymer framework with fully *sp*²-bonded carbon skeleton. *Polym Chem* 7:4176–4181
- [23] Padwal PM, Kadam SL, Mane SM, Kulkarni SB (2016) Enhanced specific capacitance and supercapacitive properties of polyaniline–iron oxide (PANI–Fe₂O₃) composite electrode material. *J Mater Sci* 51:10499–10505. doi:10.1007/s10853-016-0270-4
- [24] Huang HB, Yao JL, Chen HY, Zeng XQ, Chen CL, She X, Li L (2016) Facile preparation of halloysite/polyaniline nanocomposites via in situ polymerization and layer-by-layer assembly with good supercapacitor performance. *J Mater Sci* 51:4047–4054. doi:10.1007/s10853-016-9724-y
- [25] Yang JQ, Duan XC, Qin Q, Zheng WJ (2013) Solvothermal synthesis of hierarchical flower-like β -NiS with excellent electrochemical performance for supercapacitors. *J Mater Chem A* 1:7880–7884
- [26] Zhu XJ, Dai HL, Hu J, Ding L, Jiang L (2012) Reduced graphene oxide–nickel oxide composite as high performance electrode materials for supercapacitors. *J Power Sources* 203:243–249
- [27] Jagadale AD, Jamadade VS, Pusawale SN, Lokhande CD (2012) Effect of scan rate on the morphology of potentiodynamically deposited β -Co(OH)₂ and corresponding supercapacitive performance. *Electrochim Acta* 78:92–97
- [28] Lee SH, Kwon YT, Park SY, Cho M, Lee YK (2015) Facile synthesis of MnCO₃ nanoparticles by supercritical CO₂ and their conversion to manganese oxide for supercapacitor electrode materials. *J Mater Sci* 50:5952–5959. doi:10.1007/s10853-015-9133-7
- [29] Ke QR, Liao YY, Yao S, Song LZ, Xiong XP (2015) A three-dimensional TiO₂/graphene porous composite with nano-carbon deposition for supercapacitor. *J Mater Sci* 51:2008–2016. doi:10.1007/s10853-015-9510-2
- [30] Huo HH, Zhao YQ, Xu CL (2014) 3D Ni₃S₂ nanosheet arrays supported on Ni foam for high-performance supercapacitor and non-enzymatic glucose detection. *J Mater Chem A* 2:15111–15117
- [31] Xie LJ, Wu JF, Chen CM, Zhang CM, Wan L, Wang JL, Kong QQ, Lv CX, Li KX, Sun GH (2013) A novel asymmetric supercapacitor with an activated carbon cathode and a reduced graphene oxide–cobalt oxide nanocomposite anode. *J Power Sources* 242:148–156
- [32] Wu JH, Ouyang CB, Dou S, Wang SY (2015) Hybrid NiS/CoO mesoporous nanosheet arrays on Ni foam for high-rate supercapacitors. *Nanotechnology* 26:325401
- [33] Sun CC, Ma MZ, Yang J, Zhang YF, Chen P, Huang W, Dong XC (2014) Phase-controlled synthesis of α -NiS nanoparticles confined in carbon nanorods for high performance supercapacitors. *Sci Rep* 4:7054
- [34] Zhou WJ, Cao XH, Zeng ZY, Shi WH, Zhu YY, Yan QY, Liu H, Wang JY, Zhang H (2013) One-step synthesis of Ni₃S₂ nanorod@Ni(OH)₂ nanosheet core–shell nanostructures on a three-dimensional graphene network for high-performance supercapacitors. *Energy Environ Sci* 6:2216–2221
- [35] Ou XW, Gan L, Luo ZT (2014) Graphene-templated growth of hollow Ni₃S₂ nanoparticles with enhanced pseudocapacitive performance. *J Mater Chem A* 2:19214–19220
- [36] Chen HC, Jiang JJ, Zhang L, Xia DD, Zhao YD, Guo DQ, Qi T, Wan HZ (2014) In situ growth of NiCo₂S₄ nanotube arrays on Ni foam for supercapacitors: maximizing utilization efficiency at high mass loading to achieve ultrahigh areal pseudocapacitance. *J Power Sources* 254:249–257
- [37] Sun M, Tie JJ, Cheng G, Lin T, Peng SM, Deng FZ, Ye F, Yu L (2015) In situ growth of burl-like nickel cobalt sulfide on carbon fibers as high-performance supercapacitors. *J Mater Chem A* 3:1730–1736

- [38] De la Fuente Salas IM, Sudhakar YN, Selvakumar M (2014) High performance of symmetrical supercapacitor based on multilayer films of graphene oxide/polypyrrole electrodes. *Appl Surf Sci* 296:195–203
- [39] Bose S, Kim NH, Kuila T, Lau KT, Lee JH (2011) Electrochemical performance of a graphene–polypyrrole nanocomposite as a supercapacitor electrode. *Nanotechnology* 22:369502
- [40] Li X, Zhitomirsky I (2013) Electrodeposition of polypyrrole–carbon nanotube composites for electrochemical supercapacitors. *J Power Sources* 221:49–56
- [41] Han LJ, Tang PY, Zhang L (2014) Hierarchical $\text{Co}_3\text{O}_4@\text{-PPy@MnO}_2$ core–shell–shell nanowire arrays for enhanced electrochemical energy storage. *Nano Energy* 7:42–51
- [42] Tang CH, Yin XS, Gong H (2013) Superior performance asymmetric supercapacitors based on a directly grown commercial mass 3D $\text{Co}_3\text{O}_4@\text{Ni(OH)}_2$ core–shell electrode. *ACS Appl Mater Interfaces* 5:10574–10582
- [43] Niu LY, Li ZP, Xu Y, Sun JF, Hong W, Liu XH, Wang JQ, Yang SR (2013) Simple synthesis of amorphous NiWO_4 nanostructure and its application as a novel cathode material for asymmetric supercapacitors. *ACS Appl Mater Interfaces* 5:8044–8052
- [44] Zhu GX, Xi CY, Shen MQ, Bao CL, Zhu J (2014) Nanosheet-based hierarchical $\text{Ni}_2(\text{CO}_3)(\text{OH})_2$ microspheres with weak crystallinity for high-performance supercapacitor. *ACS Appl Mater Interfaces* 6:17208–17214
- [45] Wang YM, Zhao DD, Zhao YQ, Xu CL, Li HL (2012) Effect of electrodeposition temperature on the electrochemical performance of a Ni(OH)_2 electrode. *RSC Adv* 2:1074–1082
- [46] Xing ZC, Chu QX, Ren XB, Ge CJ, Qusti AH, Asiri AM, Al-Youbi AO, Sun XP (2014) Ni_3S_2 coated ZnO array for high-performance supercapacitors. *J Power Sources* 245:463–467
- [47] Long L, Fu WD, Yan ML, Yao YD, Wang HJ, Wang M, Liao XM, Yin GF, Huang ZB (2015) A high-performance asymmetric supercapacitor based on a directly grown nickel bicarbonate/nickel foam composite. *Electrochim Acta* 180:330–338
- [48] Sun JF, Li ZP, Wang JQ, Wang ZF, Niu LY, Gong PW, Liu XH, Wang HG, Yang SR (2013) Solvothermal synthesis of $\text{Ni(HCO}_3)_2/\text{graphene}$ composites toward supercapacitors and the faradiac redox mechanism in KOH solution. *J Alloys Compd* 581:217–222
- [49] Lang JW, Kong LB, Wu WJ, Luo YC, Kang L (2008) Facile approach to prepare loose-packed NiO nano-flakes materials for supercapacitors. *Chem Commun (Camb)* 35:4213–4215
- [50] Xiong W, Pan XX, Li Y, Chen XM, Zhu YF, Yang M, Zhang Y (2015) Hierarchical $\text{Co}_3\text{O}_4@\text{PPy}$ core/shell nanowire arrays on nickel foam for electrochemical energy storage. *Mater Lett* 157:23–26
- [51] Yan YN, Cheng G, Wang P, He DN, Chen R (2014) Facile hydrothermal selective fabrication of Ni(OH)_2 and $\text{Ni(HCO}_3)_2$ nanoparticulates and their electrochemical performances. *RSC Adv* 4:49303–49307
- [52] Huang Y, Li HF, Wang ZF, Zhu MS, Pei ZX, Xue Q, Huang Y, Zhi CY (2016) Nanostructured Polypyrrole as a flexible electrode material of supercapacitor. *Nano Energy* 22:422–438
- [53] Li R, Wang SL, Wang JP, Huang ZC (2015) $\text{Ni}_3\text{S}_2@\text{CoS}$ core–shell nano-triangular pyramid arrays on Ni foam for high-performance supercapacitors. *Phys Chem Chem Phys* 17:16434–16442
- [54] Cai DP, Liu B, Wang DD, Liu Y, Wang LL, Li H, Wang YR, Wang CX, Li QH, Wang TH (2014) Facile hydrothermal synthesis of hierarchical ultrathin mesoporous NiMoO_4 nanosheets for high performance supercapacitors. *Electrochim Acta* 115:358–363
- [55] Chen H, Zhou SX, Wu LM (2014) Porous nickel hydroxide–manganese dioxide-reduced graphene oxide ternary hybrid spheres as excellent supercapacitor electrode materials. *ACS Appl Mater Interfaces* 6:8621–8630
- [56] Yang Q, Lu ZY, Sun XM, Liu JF (2013) Ultrathin Co_3O_4 nanosheet arrays with high supercapacitive performance. *Sci Rep* 3:3537
- [57] Peng YJ, Wu TH, Hsu CT, Li SM, Chen MG, Hu CC (2014) Electrochemical characteristics of the reduced graphene oxide/carbon nanotube/polypyrrole composites for aqueous asymmetric supercapacitors. *J Power Sources* 272:970–978